Lecture Notes
Contact Mechanics and Elements of Tribology

Vladislav A. Yastrebov

CNRS, Mines Paris - PSL
CNRS UMR 7633, Centre des matériaux
Versailles, France

February 24-27, 2026

Copyright Notice

Abstract

These lecture notes cover the content of the course ″Contact Mechanics and Elements of Tribology″ that I taught for 11 years in the Master′s program ″Design of Materials and Structures″ at the Centre des Matériaux of Mines Paris.

V.A. Yastrebov
Fontainebleau - Versailles - Paris
20 February 2026

Contents

Chapter 1

Inelastic Materials

Introduction

In this chapter we will touch upon material non-linearity related to contact mechanics including elastic-plastic and viscoelastic behaviors.

1.1 Elastic-Plastic Contact

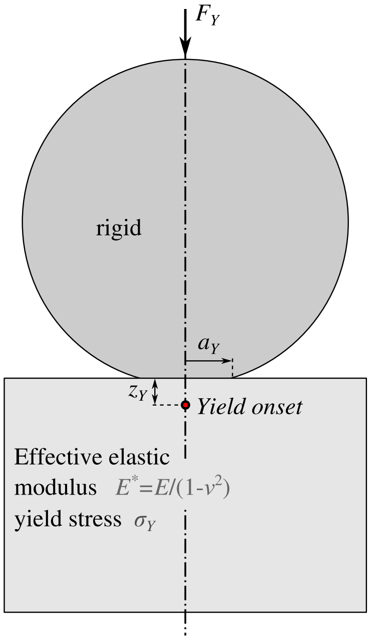

Figure 1.1: Indentation of an elastic-plastic substrate by a rigid spherical indenter and the schematic location of the point of plastic onset.

1.1.1 Onset of Plastic Yielding

Plasticity shares many traits with the friction, notably the notion of a threshold: elastic limit in plasticity and maximal frictional resistance in friction. This threshold implies that before the stress at some location does not reach this threshold, the mechanical behavior of the system remains linear. Thus, the onset of plasticity can be readily solved within the elastic theory.

Let us consider point Hertzian contact between a rigid spherical indenter and a flat elastic-plastic substrate (Figure 1.1), which is governed by von Mises plasticity with the limit of elasticity σ_Y. The stress state in the bulk depends on the Poisson's ratio. If we take a typical for metals Poisson's ratio of $\nu = 0.3$, it can then be computed that the onset of plasticity starts when the maximal pressure at the contact surface reaches

$$p_Y = 1.6\sigma_Y.$$

But be careful, the plasticity itself does not start on the surface but in the bulk at the axis of symmetry at depth

$$z_Y \approx 1.21R\frac{\sigma_Y}{E^*}$$

The force associated with this plastic onset is given by

$$F_Y \approx 0.6827\pi^3 R^2 E^* \left(\frac{\sigma_Y}{E^*}\right)^3.$$

Following the link between force and displacement d **??**, we get

$$d_Y \approx 0.6400\pi^2 R \left(\frac{\sigma_Y}{E^*}\right)^2. \tag{1.1}$$

The associated contact radius is then given by

$$a_Y = \frac{1.6\pi R}{2}\frac{\sigma_Y}{E^*}.$$

A more accurate analysis of the plastic onset is carried out in the inset below.

Plastic Onset Analysis

Remark on the onset of plasticity. In the idealized case of normal contact between parabolic surfaces, in the absence of friction and adhesion, Hertz theory allows us to predict the onset of plastic flow.

To determine the location of the onset point, which lies on the axis of symmetry, one can simply differentiate the von Mises equivalent stress σ_{eq} with respect to the normalized depth $z' = z/a$, where a is the contact radius. Along the axis of symmetry, the stress state is diagonal with $\sigma_z, \sigma_\theta = \sigma_r$ (see Figure 1.2). The von Mises stress is simply given by

$$\sigma_{\mathrm{eq}} = |\sigma_z - \sigma_x| = p_0\, m(\nu, z'), \tag{1.2}$$

where p_0 is the maximal contact pressure of the Hertzian solution and

$$m(\nu, z') = \left|(1+\nu)\,(1 - z' \arctan(1/z')) - \frac{3}{2(1+z'^2)}\right|. \tag{1.3}$$

The von Mises stress is then computed using the following expressions for the normalized stresses along the symmetry axis:

$$\frac{\sigma_z(z)}{p_0} = -\frac{1}{1+z'^2}, \tag{1.4}$$

$$\frac{\sigma_x(z)}{p_0} = \frac{\sigma_y(z)}{p_0} = (1+\nu)\,(z' \arctan(1/z') - 1) + \frac{1}{2(1+z'^2)}. \tag{1.5}$$

The von Mises stress reaches its maximum value at a depth z'^* satisfying

$$\frac{\partial \sigma_{\mathrm{eq}}}{\partial z'} = 0, \tag{1.6}$$

which reduces to

$$(1+\nu)\left(\arctan(1/z'^*) - \frac{z'}{1+z'^{*2}}\right) = \frac{3z'}{(1+z'^{*2})^2}. \tag{1.7}$$

The solution of this equation can be accurately approximated by an affine function (Figure 1.2,(b.4)):

$$z'^{*} = \frac{z^{*}}{a} \approx 0.3819 + 0.3319\,\nu. \tag{1.8}$$

The maximum normalized equivalent stress can also be approximated by another affine expression (Figure 1.2,(b.3)):

$$\max\left(\frac{\sigma_{\text{eq}}}{p_0}\right) = m(\nu, z'^{*}) \approx 0.7696 - 0.4739\,\nu. \tag{1.9}$$

If the yield strength is σ_Y, the maximum contact pressure required to initiate plastic yielding is

$$p_0^{*} = \frac{\sigma_Y}{m(\nu, z'^{*})}, \tag{1.10}$$

and the corresponding depth is

$$z^{*} = z'^{*} a^{*} = \frac{\pi z'^{*} p_0^{*} R^{*}}{2E^{*}} = \frac{\pi z'^{*} \sigma_Y R^{*}}{2E^{*} m(\nu, z'^{*})}, \tag{1.11}$$

where R^{*} is the effective radius of curvature and E^{*} is the effective elastic modulus.
From these expressions, the normalized depth of plastic onset can be approximated using (1.9) and (1.8) (Figure 1.2,(b.1)):

$$\frac{z^{*}}{R^{*}} \approx \frac{1.1999 + 1.0426\,\nu}{1.5393 - 0.9478\,\nu}\,\frac{\sigma_Y}{E^{*}}. \tag{1.12}$$

If the indenter is assumed rigid, then $E^{*} = E/(1-\nu^2)$, which yields the approximate form depending only on the Poisson's ratio of the deformable solid (Figure 1.2,(b.2)):

$$\frac{z^{*}}{R^{*}} \approx \frac{(1.1999 + 1.0426\,\nu)(1-\nu^2)}{1.5393 - 0.9478\,\nu}\,\frac{\sigma_Y}{E}. \tag{1.13}$$

From computational point of view, this analytical estimate allows one to construct an appropriate finite element mesh for elastoplastic simulations, i.e., to determine the required depth of refined elements.
Note that experimentally the onset of plasticity cannot be detected during an indentation test. If the plastic zone remains small, it does not significantly affect the loading curve.

1.1.2 Elastic-Plastic Transition

The onset of plasticity could be seen as a first transition in elastic-plastic contact. The plastic core appearing at the point of onset, under increasing load, will grow in size and will ultimately touch the surface, we will consider it to be a second transition. At even higher load, the whole (or at least the majority) of the contact zone will be plastified, which will be the third transition to fully plastic contact. These stages are visualized in Figure 1.4.

Finite element simulations allow to access all these transitions. In **??** we construct and indentation test of a single sinusoidal asperity in axisymmetric configuration (Liu and Proudhon 2016). The shape of the asperity is given by

$$z(r) = \begin{cases} \frac{h}{2}(\cos(2\pi r/\lambda) - 1), & r \le \lambda/2 \\ 0, & r > \lambda/2 \end{cases}$$

So, we can say that the height of the asperity is given by h and the extent by diameter λ. The curvature radius at the crest is given by

$$R = \frac{\lambda^2}{2\pi^2 h}$$

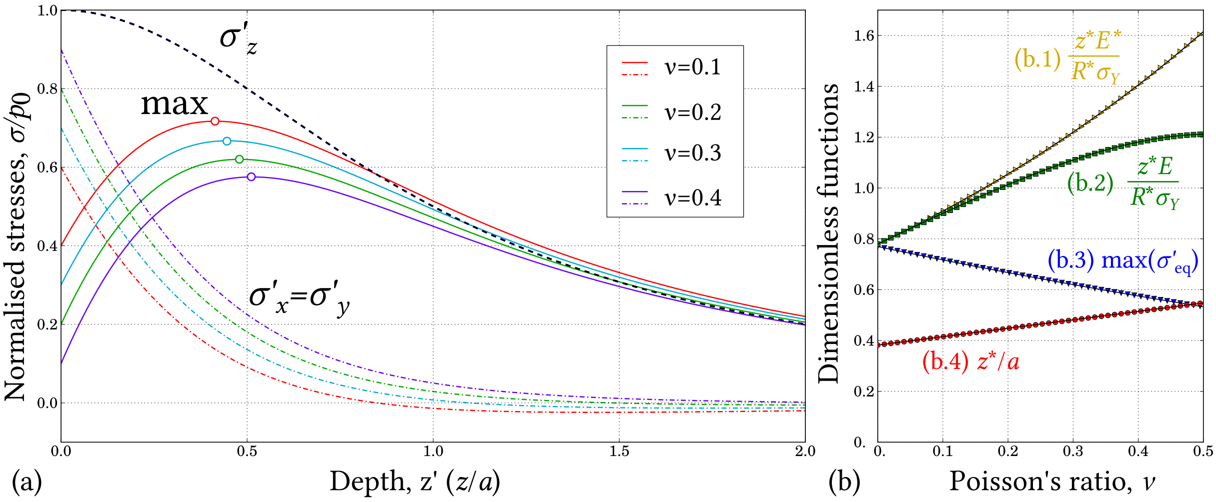

Figure 1.2: Stresses beneath Hertzian contact: (a) stress components $\sigma_x = \sigma_y$ and σ_z along the axis of symmetry; (b) dimensionless functions representing: (b.1) the normalized depth of plastic onset for a rigid indenter $z^*/R^*\,E^*/\sigma_Y$, (b.2) the normalized depth in the case of a rigid indenter $z^*/R^*\,E/\sigma_Y$, (b.3) the normalized maximum von Mises stress σ_{eq}/p_0, (b.4) the normalized depth $z'^* = z^*/a$, i.e. the solution of equation (1.7). The points correspond to exact evaluations and solid lines correspond to the approximate expressions (1.12), (1.13), (1.9), and (1.8), respectively.

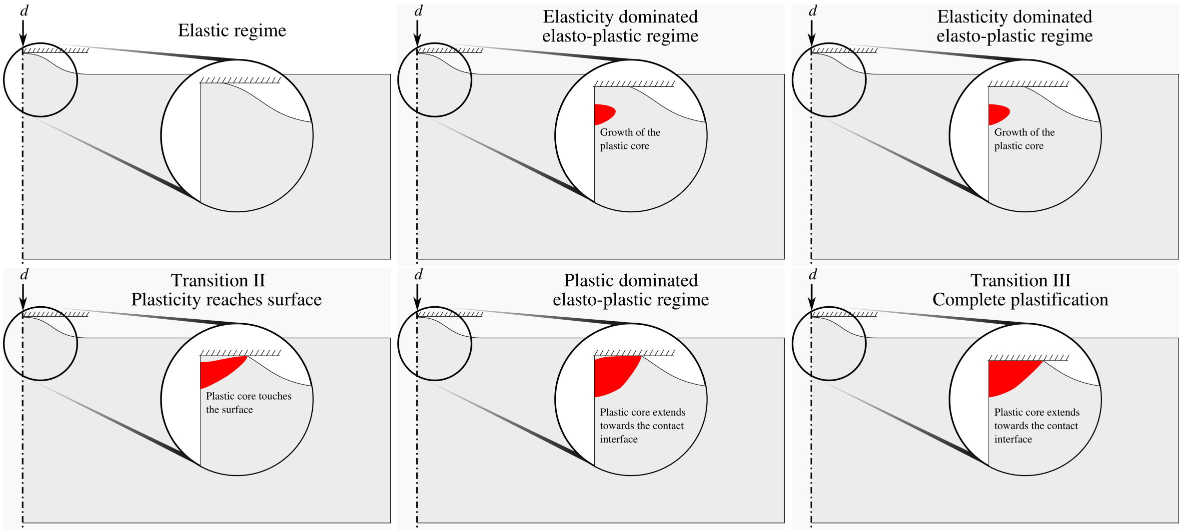

Figure 1.3: Elastic-plastic transitions in normal contact (schematic representation): from left to right (next from upper to lower): 1 – elastic regime; 2 – plastic onset (transition 1); 3 – growth of the plastic core (the deformation is still dominated by elasticity); 4 – transition II, plastic core touches the surface; 5 – plastic deformation start to dominate; 6 – most of the points are plastified in the contact interface (transition III).

We consider a geometry for which $h/\lambda = 0.1$.

The isolated asperity is brought in contact with a rigid flat indenter, the indenter is gradually decreased with vertical displacement d. When normalizing its displacement by the asperity height, we get

$$d' = \frac{d}{h} = \frac{2\pi^2 R d}{\lambda^2} = /\text{assuming } \lambda = 10h/ = \frac{2\pi^2 R d}{100h} = 10\frac{d}{\lambda}$$

We assumer a power-law hardening rule and von Mises plasticity, so that the yield surface is given by

$$f(\underline{\underline{\sigma}}, p) = \sigma_Y + E_h p^n,$$

where σ_Y is the initial yield stress, p is the equivalent plastic strain, $E_h = 830\,\text{MPa}$ is the hardening constant and n is the exponent set to 0.49. Young's modulus $E = 190\,\text{GPa}$, Poisson's ratio is $\nu = 0.3$,

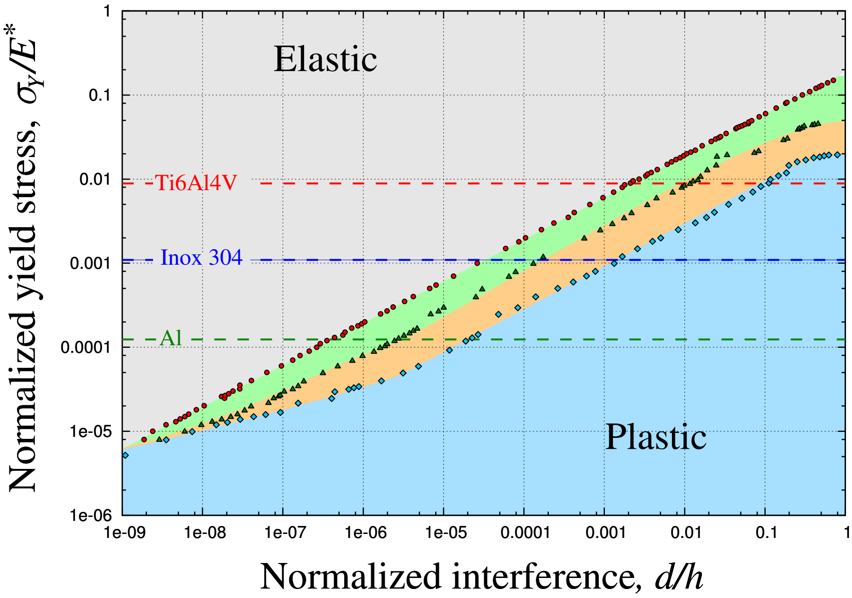

Figure 1.4: A map of elastic-to-plastic transitions for different ratios of the yield stress to the effective elastic modulus σ_Y/E^* (approximate levels of this ratio for aluminum, steel and titanium super-alloy are shown). The asymptotic $\sigma_Y/E^* \propto \sqrt{d}$ (Equation (1.1)) is preserved for all transitions. Deviations for very stiff materials are due to large deformations.

Looking on the simulation data shown in Figure 1.4, we can see that the plastic onset occurs at extremely small interferences: for model aluminum at $d/h \approx 2 \cdot 10^{-7}$ and for steel at $d/h \approx 2 \cdot 10^{-5}$. It means that if the aluminum asperity height is 1 µm, then the plastic onset will occur at $d \approx 2 \cdot 10^{-12}$ m. For a more macroscopic case of a steep bearing ball of radius $r = 5$ mm, we get the plastic onset inference of $d \approx 100$ nm and at $d \approx 5$ µm the contact will be beyond transition III, i.e. in a regime fully dominated by plastic deformation.

The growth of the plastic zone from the finite element simulations is visualized in Figure 1.5. The rapidly growing plastic core reaches the surface under the increasing load and start to spread over the contact interface, making the contact fully plastic. In this simulation the power law hardening model was used:

$$f(\underline{\underline{\sigma}}, p) = \sigma_Y + Q(1 - \exp(-bp)) \tag{1.14}$$

One can see, that in the center zone, right under the indenter the material does not plastify, this elastic island is explained by a hydrostatic dominante stress state.

1.1.3 Plastic Saturation

It is well known that the contact pressure in the developed plastic contact regime saturates at material hardness (Tabor 1951). Experimental, theoretical (Hill, Storåker, and Zdunek 1989) and numerical (Mesarovic and Fleck 1999) results are available. If we define the average pressure in contact subject to normal force N and resulting in contact radius a, we get

$$\bar{p} = \frac{N}{\pi a^2}$$

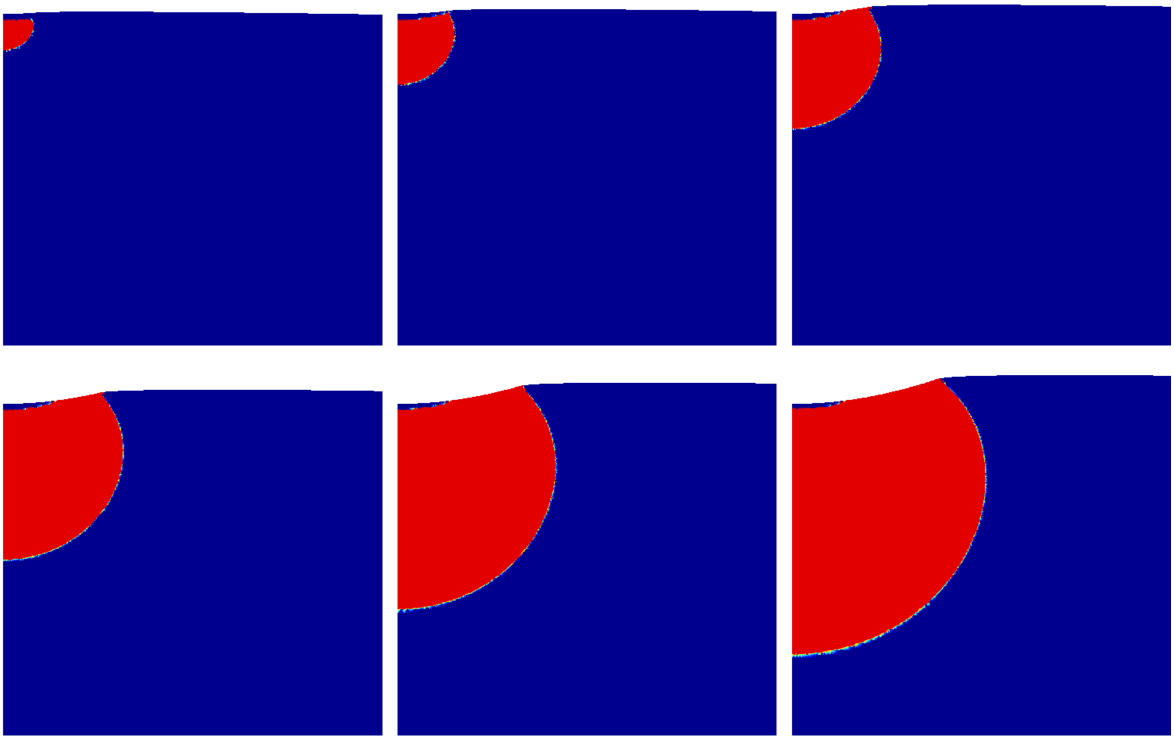

Figure 1.5: Evolution of the plastic core region (shown in red) in elastic-plastic contact with a sinusoidal asperity. The displacements are exaggerated by a factor of 100.

Figure 1.6: Evolution of the normalized pressure as a function of normalized contact radius, Equation (1.15). Adapted from (Mesarovic and Fleck 1999).

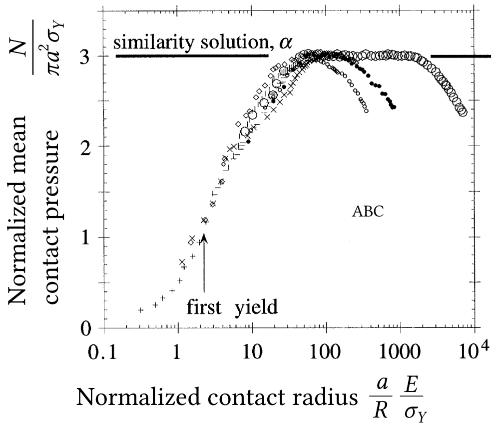

It then can be demonstrate that this pressure normalized by the yield strength gradually increases and saturates at some level close to ≈ 3:

$$\frac{\bar{p}}{\sigma_Y} = f\left(\frac{a}{R}\frac{E}{\sigma_Y}\right). \tag{1.15}$$

This dependence was explicitly visualized in (Mesarovic and Fleck 1999), see Figure 1.6. This result of pressure saturation for plastic deformation regime is at the origin of hardness testing Tabor 1951; Oliver and Pharr 1992. For the spherical indentation the pressure saturates at hardness H:

$$\boxed{\bar{p}_{\text{pl}} = H \in [2.5, 3]\sigma_Y}$$

The true level of saturation depends on the hardening. As demonstrated in (Mesarovic and Fleck 1999) for a power-law hardening, the saturation at $3\sigma_Y$ is possible, see Figure 1.6. However, other saturation values were also determined numerically. In Figure 1.7, we show finite element simulation results obtained for elastic-perfectly plastic material and elastic-plastic with exponential hardening with saturation (1.14). The results show that the rule of thumb $H \approx 3\sigma_Y$ is acceptable, but when a better accuracy is needed, this estimating has to be improved.

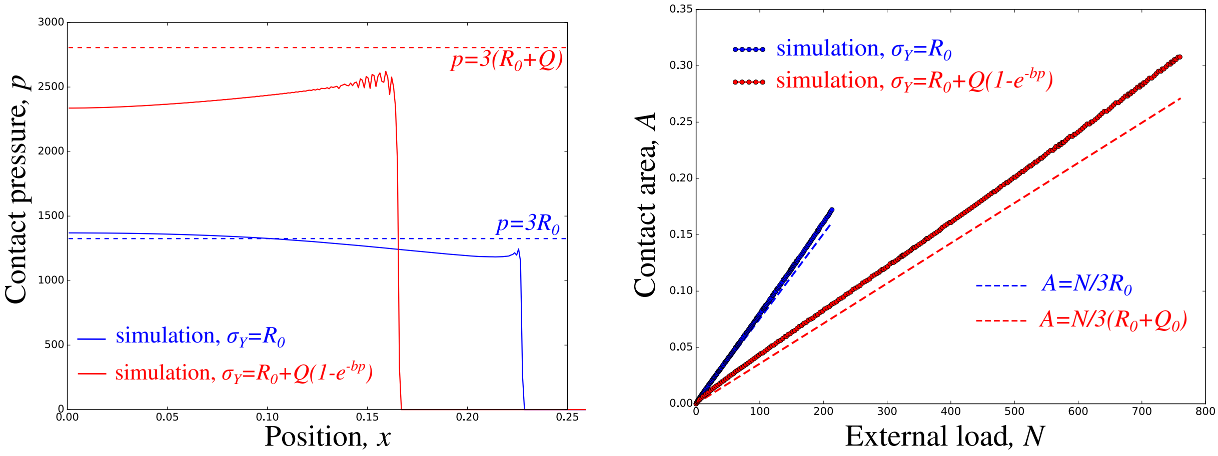

Figure 1.7: Left: contact pressure in fully plastic regime for two hardening models (perfectly plastic and exponential hardening with saturation (1.14)); Right: the growht of the contact area for the same hardening models.

Since for developed plastic deformation the pressure saturates at material hardness we can easily estimate the level of the true contact area:

$$\boxed{A = A_0 + N/H}$$

where A_0 is the elastic offset, N is the normal force and H is the material hardness. This equation normally valid for any geometry should be used with caution at microscopic scale of surface roughness because for microscopic asperity the hardness becomes size dependent, see Section 1.1.6

For relevant references on the elastic-plastic indentation, the reader is referred to studies carried out by Komvopoulos *et al.* (Kral, Komvopoulos, and Bogy 1993; Komvopoulos 1989; Z. Song and Komvopoulos 2013) and by Etsion *et al.* (Kogut and Izhak Etsion 2002; Kogut and Izhak Etsion 2003; Etsion, Kligerman, and Kadin 2005; Yuri Kadin, Yuri Kligerman, and Izhak Etsion 2006; Brizmer, Y. Kligerman, and I. Etsion 2007). Elastoplastic contact in the presence of a coating was investigated in (Sun, Bloyce, and Bell 1995; W. Song et al. 2012) using the finite element method.

1.1.4 Non-Monotone Loading

Many studies dealing with elastoplastic contact focus exclusively on the loading phase. However, the unloading phase as well as repeated contact (cyclic loading) are extremely important when considering asperity contact. Let us consider a cyclic loading of an elastic-plastic spherical deformable solid by a flat indenter subject to changing force $F(t)$. The force increases and decreases within every cycle, and the maximal value of every new cycle increased, see Figure 1.8. We carry out finite element simulations of this problem. The resulting contact area evolution is also shown in the same figure.

Figure 1.9 presents the change of the contact area with the applied force and the loading trajectory. Cycle zero is purely elastic and follows the Hertz solution. For cycles with higher load (branch 1), the contact pressure saturates at the material hardness, and the derivative of the contact area A with respect to the compressive force, $\partial A/\partial F$, remains constant. That is, the contact area evolves approximately linearly with the load,

$$A = A_0 + \frac{F}{H},$$

where H denotes the material hardness. The constant A_0 is often neglected, since it may be very small in the case of fully developed plastic contact.

The unloading phase (branch 2) is entirely elastic. However, it does not follow the Hertz relation $A \sim F^{2/3}$, because the residual curvature is no longer constant, as would be required for the Hertz solution to remain valid.

The subsequent reloading (branch 3) follows branch 2 again (as long as the response remains elastic and friction is absent). Once the load exceeds the maximum load of the previous cycle, the solution changes qualitatively and again follows the saturation curve (branch 4), and so on: elastic unloading (5), elastic reloading (6), plastic saturation (7).

This example clearly demonstrates that the contact area cannot be predicted solely from the instantaneous load. The loading history plays a fundamental role, as in all non-conservative evolutionary problems.

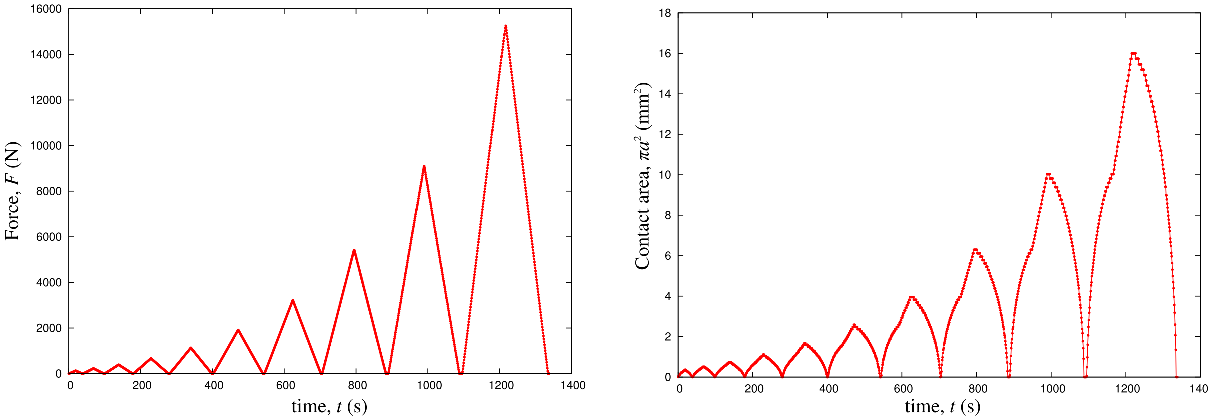

Figure 1.8: Cyclic loading of an elastic-plastic spherical deformable solid by a flat indenter subject to changing force. Left: force wrt time; right: resulting contact area wrt time.

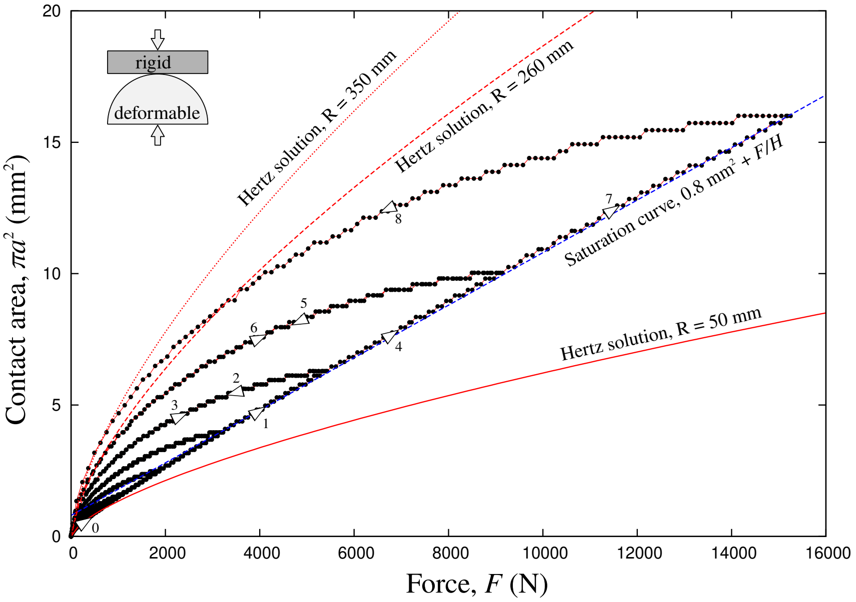

Figure 1.9: Cyclic loading of an elastic-plastic spherical deformable solid with initial radius $R = 50\,\text{mm}$ in contact with a rigid plane: contact area with respect to the normal force for the loading history depicted in Figure 1.8

In Figure 1.10 we show how the contact pressure changes gradually from Hertzian pressure to a saturated pressure with a plateau. Note however, that these illustrative results were obtained on a much coarser mesh than those presented in Figure 1.7. That is the reason why in the current illustrative example the hardness is smaller. It is also interesting to study the residual shape of the deformed spherical cap: gradually the contact surface becomes flatter and flatter, but never fully flat. We can also notice the lateral expansion – this is the result of volume conservation in plastic flow: the deformation of the cap redistributed the material on the lateral sides.

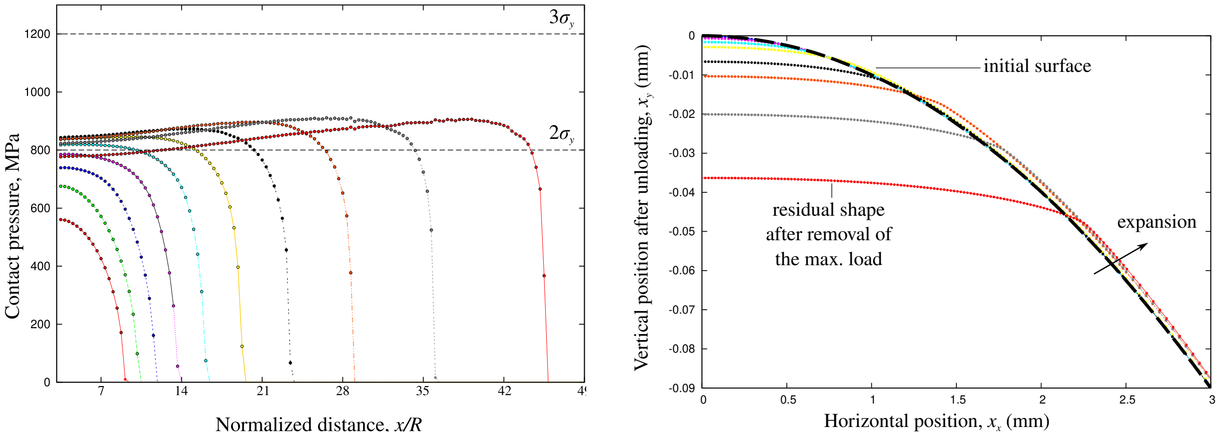

Figure 1.10: Cyclic loading of an elastic-plastic spherical deformable solid. Left: contact pressure at maximum load of every load cycle. Right: residual shape of the deformed solid.

1.1.5 Near-Surface Versus Bulk Deformation

Classical contact theory assumes that the material is homogeneous and that its mechanical properties are identical near the surface and in the bulk, Figure 1.11. In many engineering materials, however, the near-surface region differs significantly from the interior. As a result, contact-induced deformation may be governed by mechanisms that are not captured by bulk constitutive laws.

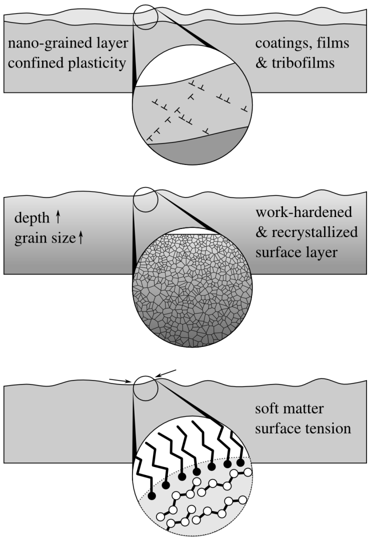

Figure 1.11: Material structure and consequently mechanical properties near the surface are different from those of the bulk material.

Surface work hardening and recrystallization. Manufacturing processes such as machining, polishing, or shot peening often produce cold-worked surface layers. These layers may exhibit refined grain structures due to severe plastic deformation and subsequent recrystallization. Since the yield stress increases with decreasing grain size (Hall-Petch effect), the near-surface region may be substantially stronger than the underlying bulk material. Classically, the Hall-Petch effect captures the link between the grain size d and the yield strength as

$$\sigma_Y = \sigma_{Y0} + \frac{k}{\sqrt{d}}.$$

Thus, naturally, the material hardness $H \approx 3\sigma_Y$ at the cold-worked surface with smaller grains becomes higher than in the bulk.

Thin coating films. Protective or functional coatings frequently have a nanocrystalline microstructure. Therefore, again the effective local hardness would be different from the bulk one.

Oxide layers. Oxides formed on metallic surfaces typically exhibit high stiffness and hardness but low fracture toughness. Under contact loading, such layers may fail by cracking thus exposing pure metal surface, which can exhibit high adhesion. An interesting experiments were presented in Rabinowicz (1965) demonstrating how the higher normal load results in breakage of surface oxides exposing clean metal and strongly increasing the friction.

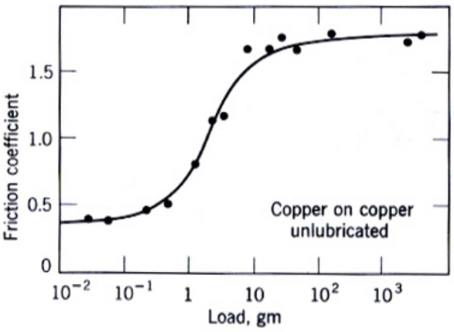

Figure 1.12: Hard film on a softer substrate, at moderate loads friction is determined by the film friction, at higher loads, the coating brakes and softer material determines the frictional properties.

Soft matter and surface tension effects. In soft polymers, gels, or biological materials, surface tension may become comparable to elastic forces. In this regime, the mechanics of contact is influenced by an intrinsic length scale

$$\ell = \frac{\gamma}{E},$$

where γ is the surface energy and E is the elastic modulus. When the contact radius is comparable to ℓ, Hertzian scaling no longer holds.

The main message here is that the contact behavior is governed by local, near surface material behavior. Therefore, material properties, often measured in the bulk, should be used with caution.

1.1.6 Indentation Size Effect

Let us return to the solution for the onset of plasticity presented in Section 1.1.1. Let us now carry out some dimensional analysis for a microscopic gold asperity coming in contact with a rigid indenter. For this system, the approximate effective modulus is $E^* \approx 96\,\text{GPa}$, the yield strength is $\sigma_y \approx 140\,\text{MPa}$, and the lattice constant $d \approx 4.1\,\text{Å}$. If the asperity curvature is $R = 1\,\mu\text{m}$, then the contact force required for the plastic onset is $F_Y = 28\,\text{nN}$, the corresponding contact radius $a_Y \approx 3.6\,\text{nm} \approx 8.8d$ and the depth is $z_Y \approx 1.8\,\text{nm} \approx 4.4d$. At such a small scale of several atoms, the continuum mechanics cannot be expected to remain valid at such scales without even hoping that the plastic behavior would follow isotropic von Mises model. Moreover, the stresses at such small scales do not follow the hertzian contact (Luan and Robbins 2005). To capture what is happening at small-scale plastic deformation, one needs to carefully take into account the fine deformation processes, such as dislocation hardening effect.

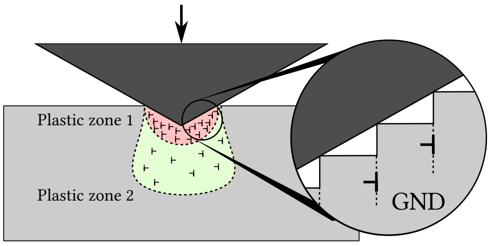

Figure 1.13: Indentation of a crystalline solid by a conical indenter creates geometrically necessary dislocations to accommodate the shape; these dislocations being confined in some volume under the indentation zone result in the increase of the yield strength.

Consider a rigid conical indentation of a crystalline solid, see Figure 1.13 as studied by Nix and Gao (1998). The key idea of the indentation size effect consists in accommodating the shape of the indenter by a series of circular loops of *geometrically necessary dislocations* (GND). Each dislocation loop creates a step of size of Burgers vector b at radial distance r thus resulting in a loop of length $2\pi r$. For an indenter of opening angle $(\pi - 2\alpha)$, for the indentation depth of h, the contact zone extends to the radius $a = h/\tan(\alpha)$, so we need to create approximately $n = h/b$ equally spaced dislocation loops of the total length $l = 2\pi(a/n + a) * n/2 = \pi a(n+1)$. If these dislocations are confined in a semi-spherical zone of radius $R = r$ under the indenter in the volume $V = 4\pi a^3/6$ (as shown in "plastic zone 1" in Figure 1.13), then the total dislocation density of GNDs is

$$\rho_{\mathrm{GND}} = \frac{l}{V} = \frac{6\pi a(h+b)}{4b\pi a^3} \propto \frac{(h+b)\tan^2(\alpha)}{bh^2} \propto \frac{1}{bh}$$

The last simplification assumes that $h \gg b$. Then using Taylor relation linking the total dislocation density with the yield strength

$$\sigma_Y = \beta\mu b\sqrt{\rho_s + \rho_{\mathrm{GND}}},$$

where ρ_s is the density of statistically stored dislocations related to the homogeneous strain, μ the shear modulus, and β is a constant of order of unity (taken to be 0.5 in (Nix and Gao 1998)), we obtain

$$\sigma_Y = \sigma_{Y0}\sqrt{1 + h_0/h}$$

where $\sigma_{Y0} = \beta\mu b\sqrt{\rho_s}$ is the yield strength without GNDs, and h_0 is a characteristic length depending on the indenter, density of statistically stored dislocations. Then assuming that H_0 for macroscopic indentation, the hardness is $H_0 = 3\sigma_{Y0}$, then the indentation depth-dependent hardness is given by

$$\boxed{H = H_0\sqrt{1 + \frac{h_0}{h}}} \tag{1.16}$$

This result due to Nix and Gao (1998) overestimates the effective GND density as they have a tendency to slide far beyond the semi-spherical zone right under the indenter (as shown in "plastic zone 2" in Figure 1.13 and in dislocation simulations Figure 1.16). Further corrections were introduced in (Feng and Nix 2004; Qiu et al. 2001) approximated the ratio of the resulting radius R of the volume storing dislocation to the contact radius through the following equation:

$$g(h) = \frac{R}{a} = 1 + \gamma\exp(-h/h_1),$$

where two constants are introduced γ and h_1. Then the resulting hardness dependence on the depth of penetration becomes

$$\boxed{H = H_0\sqrt{1 + \frac{h_0}{g(h)h}}} \tag{1.17}$$

This form then contains three constants to be experimentally determined h_0, h_1, γ. The following form introduces a threshold H_p resulting in four constants:

$$\boxed{H = H_p + (H_0 - H_p)\sqrt{1 + \frac{h_0}{g(h)h}}} \tag{1.18}$$

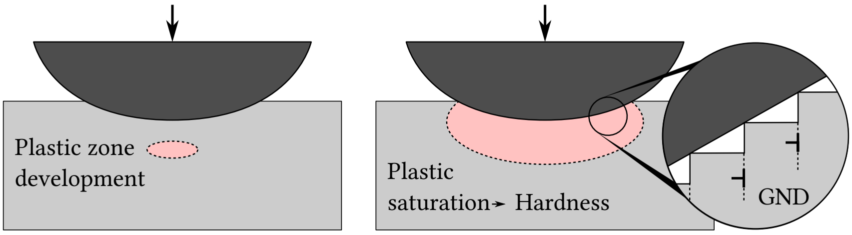

Figure 1.14: Spherical indentation with indentation size effect.

Spherical Indenter In case of spherical indenter, the indentation size effect depends not on the penetration depth but on the indenter's curvature radius (Figure 1.14): the smaller the radius, the higher the hardness. The same analysis with GNDs as was carried out with conical indenter can be carried out here resulting in the following dependence on the curvature radius R:

$$H = H_0 \sqrt{1 + \frac{R_0}{R}}.$$

It is interesting to remark that in a perfect crystal with a perfect surface, the first dislocations emerge under the indenter and then propagate into the bulk (Chang et al. 2010), snapshots of this process are shown in Figure 1.15. This initial dislocation configuration can be inserted into a dislocation dynamics code to simulate further evolution of dislocations Figure 1.16 clearly showing the zone of localization of GNDs, which can be used in phenomenological models Section 1.1.6.

Figure 1.15: Indentation of a perfect FCC crystal by a spherical indenter $R = 12\,\text{nm}$, only atoms with disturbed FCC order are highlighted allowing to see emergent dislocations. Figure adapted from (Chang et al. 2010).

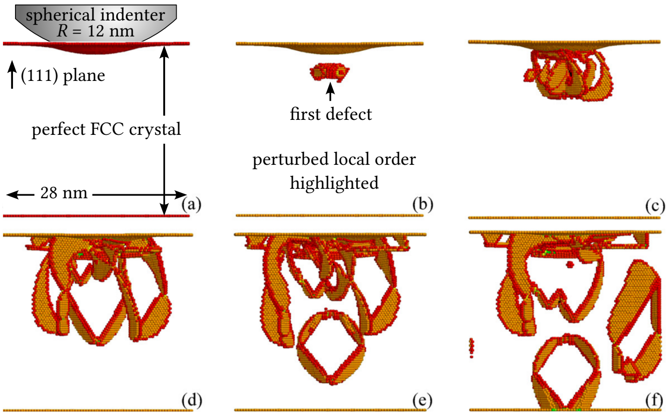

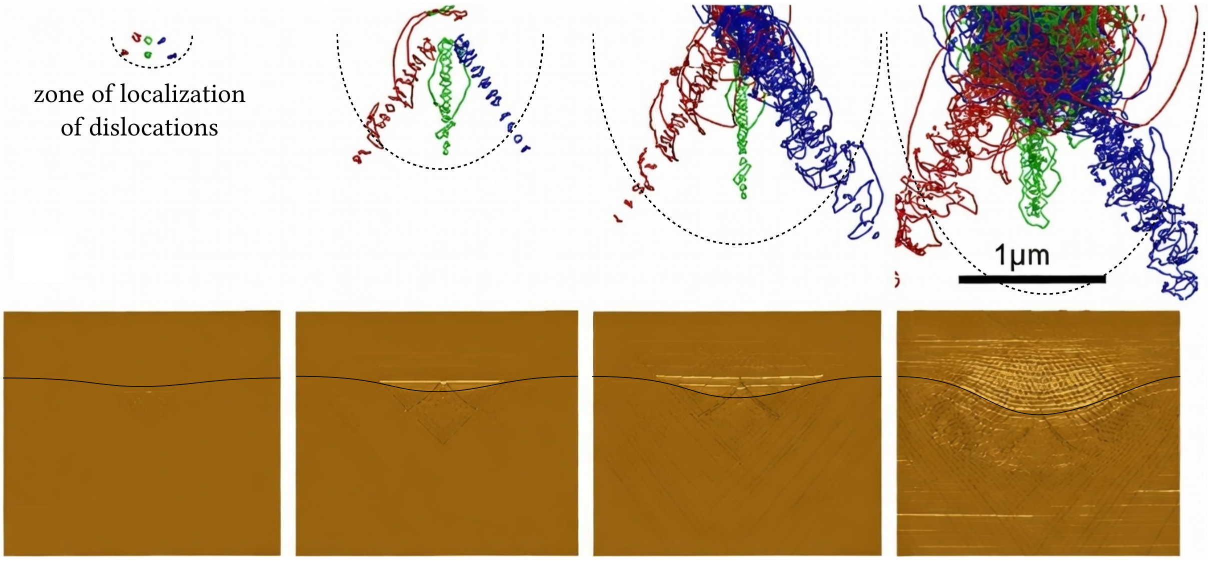

Figure 1.16: Evolution of dislocations under spherical indenter simulated with Discrete Dislocation Dynamics. Figure adapted from (Chang et al. 2010).

1.2 Viscoelastic contact

After exploring the plastic effects, we will discover the effect of viscoelasticity in contact mechanics for normal and tangential contact. Before digging into viscous effects, let us introduce the basic viscoelastic model that we will use throughout this section.

1.2.1 Generalized Maxwell Viscoelastic Model

One-Dimensional Constitutive Equations We consider the standard linear solid also known as Zener model, composed of a spring of stiffness E_∞ in parallel with a Maxwell element: a spring of stiffness E_1 in series with a dashpot of viscosity η, see Figure 1.17.

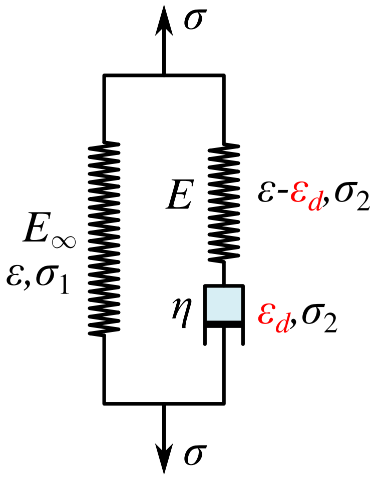

Figure 1.17: Standard linear solid (Zener model): a spring E_∞ in parallel with a Maxwell element (spring E in series with dashpot η).

Let σ denote the applied stress and ε the total strain. The total stress is the sum of stresses carried by the two branches:

$$\sigma = \sigma_1 + \sigma_2.$$

In the purely elastic branch,

$$\sigma_1 = E_\infty \varepsilon.$$

In the Maxwell branch, the stress is the same in the dashpot and the spring and the deformation decompose between them

$$\sigma_2 = \eta\dot{\varepsilon}_d, \qquad \sigma_2 = E_1(\varepsilon - \varepsilon_d),$$

where ε_d denotes the viscous strain associated with the dashpot and η is the viscosity [Pa s]. The viscous strain is the state or history variable.

Combining the stress contributions, we get

$$\sigma = E_0\varepsilon - E_1\varepsilon_d, \quad E_0 = E_\infty + E_1$$

From the equality of stresses in the Maxwell branch,

$$\eta\dot{\varepsilon}_d = E_1(\varepsilon - \varepsilon_d).$$

Introducing the relaxation time τ [s]:

$$\tau = \frac{\eta}{E_1},$$

we obtain the evolution equation for the internal variable:

$$\boxed{\dot{\varepsilon}_d = \frac{1}{\tau}\left(\varepsilon - \varepsilon_d\right),} \qquad \varepsilon_d(t \to -\infty) = 0.$$

The system therefore consists of a stress-strain relation coupled to a first-order differential equation governing the viscous strain.

If the loading is very fast compared to characteristic time $\dot{\varepsilon}\tau \gg 1$, then the material's response is elastic with fast modulus E_0, if on the opposite the loading is slow $\dot{\varepsilon}\tau \ll 1$, the material also behaves as elastic but with a softer response E_∞. In the intermediate interval $\dot{\varepsilon}\tau \sim 1$, the material fully demonstrates its viscoelastic behavior.

1.2.2 Generalized Maxwell Model (Wiechert Model)

The generalized Maxwell model consists of several Maxwell elements connected in parallel with a purely elastic spring of stiffness E_∞. Each Maxwell branch is composed of a spring of stiffness E_i in series with a dashpot of viscosity η_i.

Let ε denote the total strain. The total stress is the sum of contributions of all branches:

$$\sigma = \sigma_\infty + \sum_i \sigma_i.$$

The purely elastic branch gives

$$\sigma_\infty = E_\infty\varepsilon.$$

Each Maxwell branch satisfies

$$\sigma_i = E_i(\varepsilon - \varepsilon_d^i), \qquad \eta_i\dot{\varepsilon}_d^i = \sigma_i,$$

where ε_d^i is the viscous strain in the i-th dashpot.

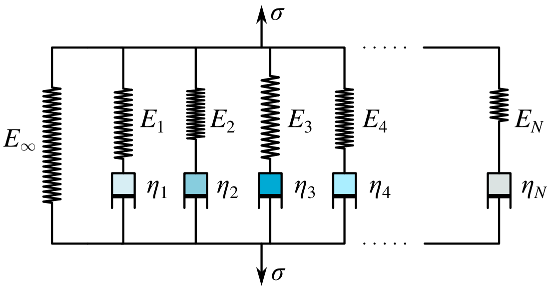

Figure 1.18: Generalized Maxwell (Wiechert) model: parallel spring E_∞ and multiple Maxwell branches (E_i, η_i).

Combining these relations yields

$$\sigma = E_0\varepsilon - \sum_i E_i\varepsilon_d^i, \qquad E_0 = E_\infty + \sum_i E_i$$

The internal variables evolve according to

$$\boxed{\dot{\varepsilon}_d^i = \frac{1}{\tau}\left(\varepsilon - \varepsilon_d^i\right),} \qquad \tau_i = \frac{\eta_i}{E_i}, \qquad \varepsilon_d^i(t \to -\infty) = 0.$$

1.2.3 Harmonic Loading: Storage and Loss Moduli

To characterize viscoelastic behavior in the frequency domain, consider a harmonic strain input

$$\varepsilon(t) = \varepsilon_0 \sin(\omega t),$$

where ε_0 is the strain amplitude and ω is the angular frequency.

For a linear viscoelastic material, the resulting stress is also harmonic, but generally phase-shifted:

$$\sigma(t) = \sigma_0 \sin(\omega t + \delta),$$

where δ is the phase lag between stress and strain.

Storage and Loss Moduli

Using trigonometric identities, the stress may be rewritten as

$$\sigma(t) = \sigma_0 \left[\sin(\omega t) \cos\delta + \cos(\omega t) \sin\delta\right].$$

It is therefore convenient to define

$$E'(\omega) = \frac{\sigma_0}{\varepsilon_0} \cos\delta, \qquad E''(\omega) = \frac{\sigma_0}{\varepsilon_0} \sin\delta,$$

where

- $E'(\omega)$ is the *storage modulus*, representing the elastic (energy-storing) component,
- $E''(\omega)$ is the *loss modulus*, representing the viscous (energy-dissipating) component.

These moduli take the following form:

$$E'(\omega) = E_\infty + E_0 \frac{\omega^2\tau_0^2}{1+\omega^2\tau_0^2} \tag{1.19}$$

$$E''(\omega) = E_0 \frac{\omega\tau}{1+\omega^2\tau_0^2} \tag{1.20}$$

The stress response can then be expressed as

$$\sigma(t) = \varepsilon_0 \left[E'(\omega) \sin(\omega t) + E''(\omega) \cos(\omega t)\right]$$

or alternatively as

$$\sigma(t) = E'(\omega)\varepsilon(t) + E''(\omega)\frac{\dot{\varepsilon}(t)}{\omega}.$$

In Figure 1.19, we show how the storage and loss moduli change with the excitation frequency.

In Figure 1.20 we show a simulation of a tension-compression test on a viscoelastic cube at different frequencies f, note that $\omega = 2\pi f$.

Loss Factor

In Dynamic Mechanical Analysis (DMA)[1], the ratio

$$\tan\delta = \frac{E''(\omega)}{E'(\omega)}$$

is commonly used. The quantity $\tan\delta$ is called the *loss factor* and measures the relative importance of viscous dissipation compared to elastic storage.

Energy interpretation.

Over one loading cycle, the energy stored elastically is proportional to E', while the energy dissipated per cycle is proportional to E''. A purely elastic solid has $\delta = 0$ and $E'' = 0$, whereas a purely viscous fluid has $\delta = \pi/2$ and $E' = 0$.

---

[1] DMA is an experimental technique to construct storage and loss moduli of viscoelastic solids: a harmonic loading is applied and the material response assumed to be also harmonic is measured.

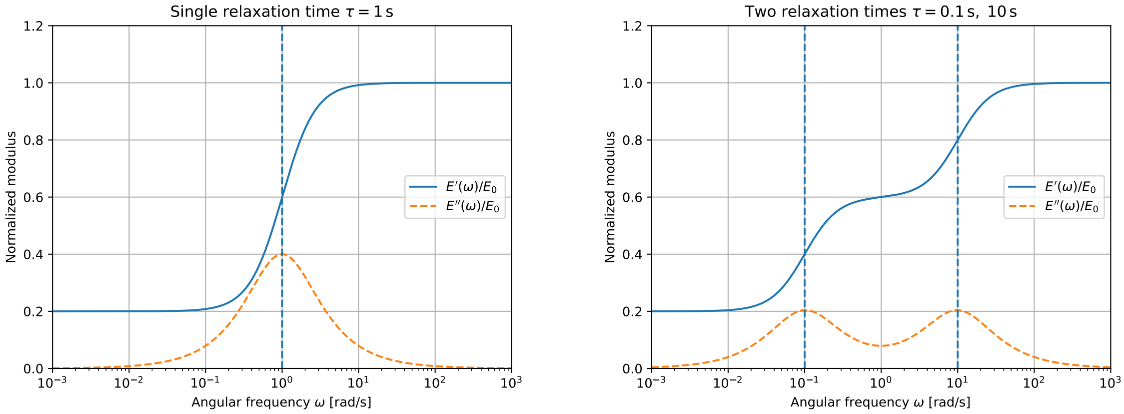

(a) (b)

Figure 1.19: Storage E' and loss E'' viscoelastic moduli: (a) for a single relaxation time $\tau = 1\,\mathrm{s}$; (b) for two relaxation times $\tau_1 = 0.1\,\mathrm{s}$, $\tau_1 = 10\,\mathrm{s}$.

Complex Representation

It is convenient to introduce the complex strain

$$\varepsilon(t) = \Re\left\{\varepsilon_0 e^{i\omega t}\right\},$$

where $\Re(\bullet)$ denotes the real part of a complex number.

The stress response can then be written as

$$\sigma(t) = \Re\left\{E^*(\omega)\,\varepsilon_0 e^{i\omega t}\right\},$$

where the complex modulus is defined as

$$\boxed{E^*(\omega) = E'(\omega) + iE''(\omega)}.$$

The magnitude of the complex modulus is

$$|E^*| = \sqrt{E'^2 + E''^2},$$

and the phase angle satisfies

$$\tan\delta = \frac{E''}{E'}.$$

Thus, viscoelasticity in the frequency domain is completely characterized by the complex modulus $E^*(\omega)$, or equivalently by the pair (E', E'').

1.2.4 Sliding Over a Viscoelastic Substrate

Here we study sliding of a rigid circular indenter over a viscoelastic substrate of finite thickness (Figure 1.21). The substrate is loaded vertically at rate w and then sheared to the left at a constant speed v as shown in Figure 1.23. Because of the viscous dissipation in intermediate sliding velocity range, even in absence of surface friction, the viscoelastic material resists to sliding. The volumetric dissipation makes the contact pressure asymmetric shifting the peak towards the leading edge and thus, when integrated over the contact zone and projected on the tangential direction a non-zero frictional force emerges.

To explain this phenomenon, let us consider a single asperity making a contact of radius (or half-width) a with viscolastic substrate. If the sliding speed is v, then the characteristic time of deformation

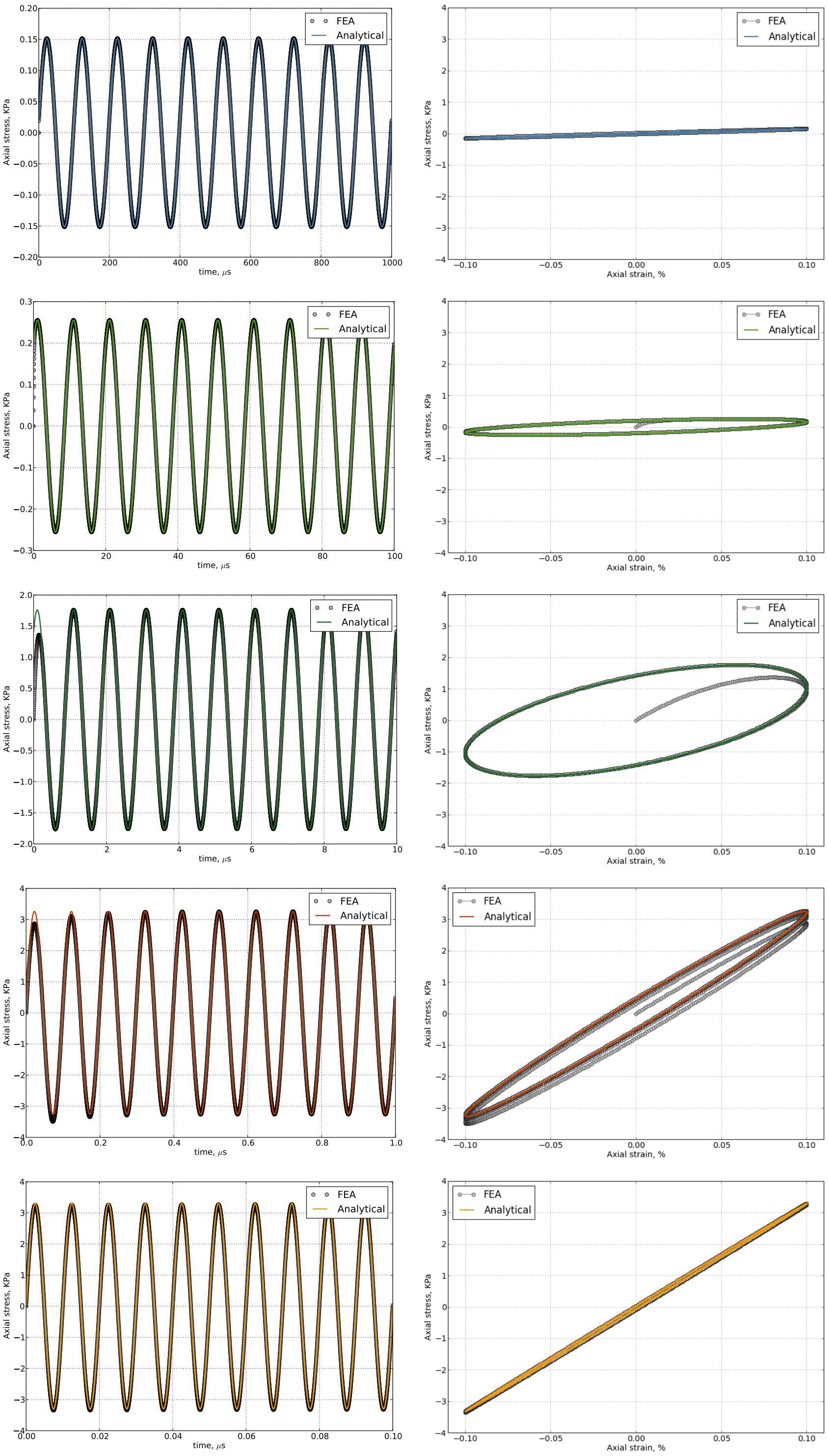

Figure 1.20: Tension-compression of a cube subject to a harmonic loading with frequencies (from top to bottom): $f\tau = \{10^{-3}, 10^{-2}, 10^{-1}, 1, 10\}$, left column – stress wrt time, right column – stress-strain trajectory. Note that all trajectories start from a relaxed state $\varepsilon = 0$, $\sigma = 0$ but rapidly converge to the stationary response.

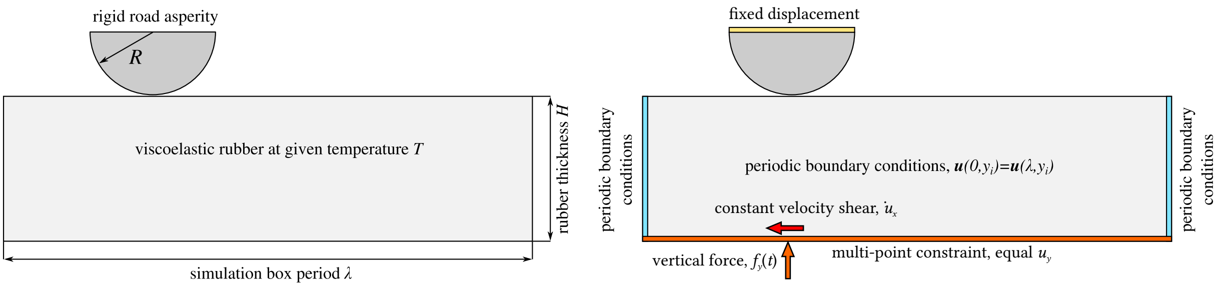

Figure 1.21: Problem of a rigid indenter sliding over a viscoelastic substrate.

Figure 1.22: Loading history for an indenter sliding over a viscoelastic substrate.

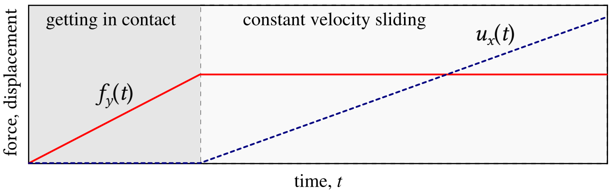

under the asperity is $T \approx 2a/v$ and the angular frequency $\omega_a = v/(2a)$. Therefore, if sliding velocity and the contact size correspond to the characteristic relaxation time of the Zener model

$$\frac{2a}{v} \approx \tau,$$

then the dissipation would be maximal. Realistic materials, however, have a broad spectrum of relaxation times, thus resulting in a large spectrum of velocities resulting in high frictional dissipation. However, the key feature of rubber friction is small dissipation for very slow sliding velocities and sometimes for very fast velocities too, see simulation results in **??** for illustration.

Figure 1.23: Frictional resistance defined as stabilized tangential force normalized by the normal force max(T/F) for different sliding velocities and three normal contact forces F.

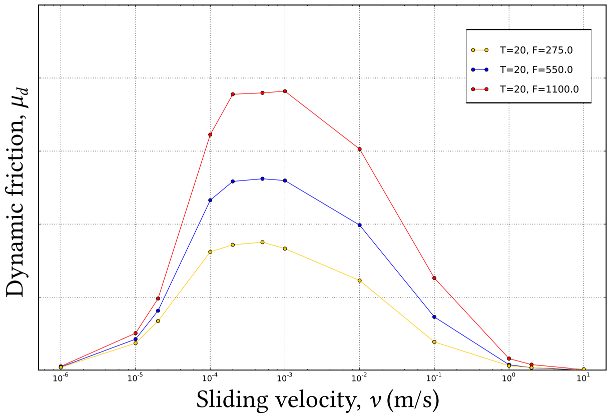

Another interesting effect in viscoelastic friction is the transition from normal loading and hold to sliding. If loading is very fast and hold time is very short, compared to the characteristic sliding rate, the frictional force gradually increases before reaching the limit characterized by material behavior at frequency $\omega_a = v/(2a)$ – this is the case of frictional strengthening. However, if the loading is slow or the hold time is long, then to transit to the steady sliding, friction has to overcome a barrier resulting from a too deep penetration of the indenter. In this situation, the friction increases first up to reaching the maximal value, which can be considered as a static limit and then gradually decays towards the same stationary dynamic value (see Figure 1.24) – this situation results in softening frictional behavior.

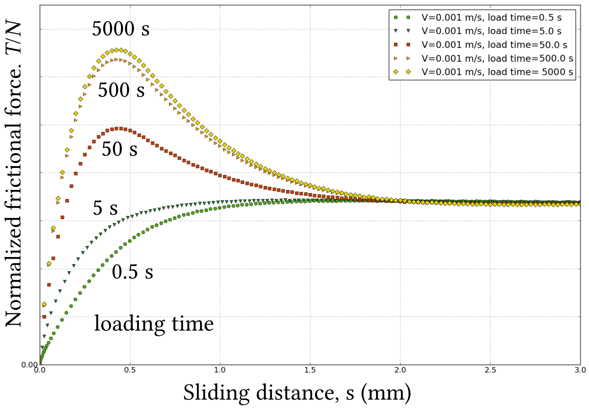

Figure 1.24: Frictional resistance evolution for different loading histories: very slow normal loading creates a frictional barrier resulting in softening frictional evolution.

Bibliography

Brizmer, V., Y. Kligerman, and I. Etsion (2007). "Elastic–plastic spherical contact under combined normal and tangential loading in full stick". In: *Tribology Letters* 25.1, pp. 61–70.

Chang, Hyung-Jun et al. (2010). "Multiscale modelling of indentation in FCC metals: From atomic to continuum". In: *Comptes Rendus Physique* 11.3-4, pp. 285–292.

Etsion, I, Y Kligerman, and Y Kadin (2005). "Unloading of an elastic–plastic loaded spherical contact". In: *International Journal of Solids and Structures* 42.13, pp. 3716–3729.

Feng, Gang and William D Nix (2004). "Indentation size effect in MgO". In: *Scripta materialia* 51.6, pp. 599–603.

Hill, R., B. Storåker, and A. B. Zdunek (1989). "A theoretical study of the Brinell hardness test". In: *Proc. R. Soc. Lond. A* 423, pp. 301–330.

Kadin, Yuri, Yuri Kligerman, and Izhak Etsion (2006). "Multiple loading–unloading of an elastic–plastic spherical contact". In: *International journal of solids and structures* 43.22-23, pp. 7119–7127.

Kogut, Lior and Izhak Etsion (2002). "Elastic-plastic contact analysis of a sphere and a rigid flat". In: *Journal of applied Mechanics* 69.5, pp. 657–662.

— (2003). "A finite element based elastic-plastic model for the contact of rough surfaces". In: *Tribology transactions* 46.3, pp. 383–390.

Komvopoulos, K (1989). "Elastic-plastic finite element analysis of indented layered media". In: *Journal of Tribology* 111.3, pp. 430–439.

Kral, ER, K Komvopoulos, and DB Bogy (1993). "Elastic-plastic finite element analysis of repeated indentation of a half-space by a rigid sphere". In: *Journal of applied mechanics* 60.4, pp. 829–841.

Liu, Ming and Henry Proudhon (2016). "Finite element analysis of contact deformation regimes of an elastic-power plastic hardening sinusoidal asperity". In: *Mechanics of Materials* 103, pp. 78–86.

Luan, B. and M. O. Robbins (2005). "The breakdown of continuum models for mechanical contacts". In: *Nature* 435, pp. 929–932.

Mesarovic, Sinisa Dj and Norman A Fleck (1999). "Spherical indentation of elastic–plastic solids". In: *Proceedings of the Royal Society of London A: Mathematical, Physical and Engineering Sciences* 455.1987, pp. 2707–2728.

Nix, William D and Huajian Gao (1998). "Indentation size effects in crystalline materials: a law for strain gradient plasticity". In: *Journal of the Mechanics and Physics of Solids* 46.3, pp. 411–425.

Oliver, Warren Carl and George Mathews Pharr (1992). "An improved technique for determining hardness and elastic modulus using load and displacement sensing indentation experiments". In: *Journal of materials research* 7.6, pp. 1564–1583.

Qiu, X et al. (2001). "Effect of intrinsic lattice resistance in strain gradient plasticity". In: *Acta Materialia* 49.19, pp. 3949–3958.

Rabinowicz, E. (1965). *Friction and Wear of Materials*. Wiley.

Song, Wenping et al. (2012). "Plastic yield inception of an indented coated flat and comparison with a flattened coated sphere". In: *Tribology International* 53, pp. 61–67.

Song, Z and K Komvopoulos (2013). "Elastic–plastic spherical indentation: deformation regimes, evolution of plasticity, and hardening effect". In: *Mechanics of Materials* 61, pp. 91–100.

Sun, Y, A Bloyce, and T Bell (1995). "Finite element analysis of plastic deformation of various TiN coating/substrate systems under normal contact with a rigid sphere". In: *Thin Solid Films* 271.1-2, pp. 122–131.

Tabor, David (1951). *The hardness of metals*. Oxford University Press.